Numerical Effects in the Simulation of Ginzburg Landau Models for Superconductivity *

Walter B. Richardson, Anand L. Pardhanani, Graham F Carey,
and Alexandre Ardelea

Texas Institute for Computational and Applied Mathematics,
The University of Texas at Austin Austin, Texas, 78712 USA

Abstract

Inadequate spatial mesh resolution for simulation of the time dependent Ginzburg-Landau equations is shown to give rise to spurious solutions. Phenomenological studies to examine the effect of the physical parameters and boundary conditions in 2D and 3D are presented to illustrate the solution structure and to highlight nonlinear effects related to evolving vortex patterns. We illustrate and explore this issue further by considering a related simplified model in which the number of vortices is equal to the "winding number" that is associated with the applied boundary conditions. Using this model we demonstrate that the solution structure is nonunique for several values of winding number.

1 INTRODUCTION

Mathematical modeling and simulation have become an essential part of engineering analysis and design in the semiconductor industry, and similar needs are evident for superconducting microelectronics. Progress in the fabrication of superconductors with critical temperatures above 100K, coupled with recent advances in cryocooler technology have created opportunities for manufacturing practical superconducting electronic devices [1] [2] [3]. The application areas are very broad, ranging from filters for microwave and wireless communications, to junction devices for metrology, sensors and detectors, to Superconductive Quantum Interference Devices (SQUIDs) as ultra-sensitive sensors for microelectronics and medicine [4] [5]. Particularly attractive for the near term are the Rapid Single Flux Quantum Logic (RSFQL) devices for ultra-fast signal processing and supercomputing [6]. To realize these goals, it is important to understand the transient behavior and steady state solution structure for the magnetic flux in superconductors, and to carry out related phenomenological and design studies.

Mathematical models for this class of problems exhibit complex solution behavior in the form of multiple "vortices" that form and evolve to distinct steady state solution patterns.

*supported by NSF grant 791AT-51067A

Moreover, the dynamical behavior of the solutions to these models is not yet well understood. These transient and steady state problems are difficult to approximate numerically and lead to computationally intensive simulations. Many superconductivity simulation studies in the literature have been directed to approximating the steady state problem rather than time-accurate transient simulation. The most widely used approach in engineering and science for solving a steady state problem is to discretize the steady state governing equations and then use a nonlinear iterative algorithm such as Newton's method. This strategy fails if the initial iterate is not sufficiently accurate (e.g., if it is outside the domain of attraction of the iterative method). Moreover, multiple solution states are possible and inadequate meshes can generate false solution branches [35]. Continuation schemes in a physical parameter, incremental approximation of boundary conditions or field strength, or other similar strategies can alleviate this difficulty but must deal with the complications of turning points and bifurcation points. These can be addressed using arc length continuation. Other approaches such as direct nonlinear descent solution of the steady problem may also be applicable [7]. Some of the difficulties concerning the convergence of the nonlinear algorithms and multiple solution branches are circumvented if, instead, a transient problem is posed and then integrated to a steady state. Moreover, extrapolation of the solution from the previous timestep provides a good starting iterate for the next timestep solve, so this solution scheme is often quite robust. If the transient solution is not of interest, then time accuracy is not required and one can elect to construct integration schemes and algorithms that have extended domains of stability, and will accelerate the simulation by taking larger timesteps. One can also use continuation ideas within this context to reduce computation time and can treat the boundary conditions in a similar vein to accelerate convergence to the steady-state, as demonstrated in some of the numerical studies carried out here.

These time-integration strategies for steady state solves become even more appealing when one is also interested in a simulation strategy that can provide time accurate solutions to the transient problem and perform dynamic sensitivity studies. In this case, it is obviously possible to have in one algorithm and simulator, both the time-accurate transient capability and the accelerated steady solver. We have developed some of the basic ideas underlying this approach in previous work [8], [9]. For these reasons, in the present work we consider the development of an analysis capability and simulation framework for both the transient and steady state problems, using algorithms based on the Time Dependent Ginzburg-Landau (TDGL) model [10], [11]. More importantly, in the present work this enables us to perform fundamental simulation studies of the nonlinear dynamics as vortices in the order parameter form and evolve. This also provides an improved understanding of the sensitivity to mesh resolution and to boundary conditions, and to barrier effects at the boundaries as the vortices enter or leave the domain.

Of particular interest is the sensitivity of simulations to mesh resolution and to nonlinear hysteresis effects as the field is increased and then decreased on a given mesh. These mesh and barrier effects have apparently not received adequate attention previously and raise concerns about the validity of some of the results in the literature. Such issues are becoming especially significant in TCAD, since the design cycle is necessarily of short duration. As the device dimensions shrink or new materials and concepts enter the technology, the underlying physical models become more complex. Thus, the need for fast, accurate, reliable simulation results using efficient algorithms on high resolution grids is becoming increasingly important.

To explore the sensitivity of the behavior to the nonlinear model we also consider a related simpler model for which the number of vortices is known *a priori* to be equal to the "winding number" associated with the boundary condition. Numerical studies reveal a similar mesh sensitivity, again leading to false solution patterns.

2 Ginzburg-Landau Theory and Physical Models

The behavior of superconductors in a magnetic field and close to the critical temperature is qualitatively well predicted by the Ginzburg Landau (GL) phenomenological theory [12] and related models. This theory combines thermodynamics, electrodynamics and experimental observations in an attempt to describe the equilibrium state of the superconductor in terms of a space-dependent order parameter ψ and an electromagnetic field (vector potential $\mathbf{A}$). One of the most interesting consequences of the GL theory was discovered by Abrikosov [13] who studied the superconductive properties of metals with short (normal state) mean free path. He found that, for an infinite superconductor with κ (the Ginzburg Landau parameter defined below) $> 1/\sqrt{2}$ and external applied fields H larger than a critical value H_{c1}, the magnetic field lines penetrate the superconductor in the form of localized vortices with strong depletions of the order parameter at their core $|\psi| \simeq 0$. He also showed that the second order phase transition to the normal state takes place at a value $H_{c2}(> H_{c1})$. Later, it was shown by Gorkov [14], that the GL equations could be derived from the microscopic theory as developed by Bardeen, Cooper and Schrieffer (BCS) [15] for behavior in the vicinity of the critical temperature. Generalizations of the Ginzburg-Landau equations with flux flow and time-dependent order parameter were developed subsequently by Stephen and Suhl [16], Anderson et al. [17], Jakemin and Pike [18], Schmid [10], Gor'kov and Elihasberg [11] and others, based on the Gor'kov microscopic formulation [14], [19], [20]. Within the GL phenomenological framework, several variants to the basic models have been developed to study specific properties of superconductors. This remains an active research topic since the macroscopic models are derived under different assumptions from microscopic theory. In fact, one of the important uses of simulation is for comparative validation of different models against experiment. In the present work we focus on finite domain and discretization mesh effects in numerical modeling of these types of problems. Of related interest are the phenomena associated with barrier effects, boundary conditions, and the influence of domain size and applied field.

From the microscopic description given in [10] and for slowly varying applied fields, the time-dependent GL equations provide a useful mathematical model, and can be expressed in the form [21], [22], [23]

$$\gamma \left(\frac{\partial \psi}{\partial t} + \frac{2ie\phi\psi}{\hbar} \right) = -\alpha\psi - \beta|\psi|^2\psi - \frac{1}{4m_e}\left(i\hbar\nabla + \frac{2e}{c}\mathbf{A} \right)^2 \psi \tag{1}$$

$$\begin{aligned} \frac{4\pi\sigma}{c}\left(\frac{1}{c}\frac{\partial \mathbf{A}}{\partial t} + \nabla\phi \right) &= -\frac{2\pi e}{m_e c}\left[\psi^* \left(i\hbar\nabla + \frac{2e}{c}\mathbf{A} \right)\psi + \psi\left(i\hbar\nabla - \frac{2e}{c}\mathbf{A} \right)\psi^* \right] \\ &\quad -\nabla\times\nabla\times\mathbf{A} + \nabla\times\mathbf{H_e} \end{aligned} \tag{2}$$

where, $\psi(\mathbf{r},t)$ is the order parameter related to the the density of superconductive electrons and $\mathbf{A}(\mathbf{r})$ and $\phi(\mathbf{r})$ are the vector and scalar potentials respectively. $\mathbf{H_e}$ is the external applied magnetic field; α and β are temperature dependent coefficients entering the Ginzburg-Landau expression for the condensation energy of the superconductor [24]; γ is a time relaxation factor; σ represents the normal conductivity; m_e and e are the electron mass and electron charge respectively. For $H_e < H_{c1}$ the material is fully superconductive with $|\psi| = 1$ and expels the magnetic flux completely, whereas for $H_e > H_{c2}$ the superconductive state is destroyed so $|\psi| = 0$ and the magnetic flux penetrates the material completely. Between these limits, fine scale "vortices" are present in the superconductor. For infinite superconductors and constant applied magnetic field, the steady state equilibrium is characterized by vortices forming a regular triangular pattern. The next lowest energy configuration consists of a regular square array [13]. During the transient, the vortices migrate and organize into these patterns as the steady state is approached. For finite domains, a surface barrier effect known as the Bean-Livingston barrier [25], inhibits vortices from "entering" the domain unless $H_{c1} < H_{barr} < H_e < H_{c2}$.

The evolution and steady state structure of the vortex patterns for finite domains is a subject of debate and has not been systematically explored. The barrier effect mentioned above is important to the behavior and structure of the pattern in the steady state, as well as the stability of the steady state to "off-design" transient perturbations which are also readily studied with the present dual-mode algorithm. The ability to simulate the boundary layer penetration in the transient problem and the pattern structure in the steady state case is also dependent on selecting the mesh and domain scaling appropriately with respect to the characteristic length scales of the problem. Of particular note in the present work is the investigation of mesh resolution effects for this model and for a related model in this general class. The quantity $\kappa = \lambda/\xi$ is known as the the Ginzburg-Landau parameter and represents the ratio of two important characteristic lengths of the model: 1) the coherence length $\xi = (\hbar/4m_e|\alpha|)^{\frac{1}{2}}$ which measures the decay length of the order parameter and 2) the penetration depth $\lambda = (2m_e\beta c^2/16\pi e^2|\alpha|)^{\frac{1}{2}}$ which corresponds to the depth to which the magnetic field penetrates the superconductor [24]. Quantities $\tau_\psi = \gamma/|\alpha|$ and $\tau_A = (m_e\beta\sigma)/(2e^2|\alpha|)$ can be viewed as relaxation times for the order parameter and for the current respectively. The particular assumptions made at the level of the microscopic theory with regard to the nature of the superconductor determine the relationship between σ, γ, ξ, λ, T_c (the critical temperature) and other relevant quantities [10].

In the numerical experiments, we consider the case of a superconductor surrounded by vacuum. At the boundary, the normal component of the current vanishes and the tangential field is subject to a Maxwell-type boundary condition such as:

$$(\frac{\hbar}{i}\nabla - 2e\mathbf{A})\psi \cdot \hat{\mathbf{n}} = 0 \qquad (\nabla \times \mathbf{A}) \times \hat{\mathbf{n}} = \mathbf{H_e} \times \hat{\mathbf{n}} \tag{3}$$

In the main mathematical model that we investigate, the relevant variables are scaled as follows

$$\psi \rightarrow \sqrt{\frac{|\alpha|}{\beta}}\,\psi' \;\;,\;\; x \rightarrow \lambda\, x' \;\;,\;\; t \rightarrow \tau\, t' \;\;,\;\; \mathbf{A} \rightarrow \sqrt{2}H_c\lambda\,\mathbf{A}' \;\;,\;\; \phi \rightarrow \frac{|\alpha|}{\gamma e_s}\,\phi' \tag{4}$$

with $H_c = H_{c2}/(\sqrt{2}\kappa)$ and the other details given in [22], [26]. For the problems considered here, a gauge is specified such that the scalar potential $\phi = 0$ in the superconductor bulk domain Ω and the term $\mathbf{A}\psi \cdot \hat{\mathbf{n}} = 0$ in the boundary condition on $\partial\Omega$ [27], [28]. Once the scaling is performed, the TDGL equations take the form [23], [27], [28], [29]:

$$\frac{\partial \psi}{\partial t} = -\left(-\frac{i}{\kappa}\nabla - \mathbf{A}\right)^2 \psi - |\psi|^2\psi + \psi \tag{5}$$

$$\frac{\partial \mathbf{A}}{\partial t} = -\frac{i}{2\kappa}(\psi^*\nabla\psi - \psi\nabla\psi^*) - |\psi|^2\mathbf{A} - \nabla \times \nabla \times \mathbf{A} + \nabla \times \mathbf{H_e} \tag{6}$$

with boundary conditions

$$\nabla\psi \cdot \hat{\mathbf{n}} = 0 \qquad (\nabla \times \mathbf{A}) \times \hat{\mathbf{n}} = \mathbf{H_e} \times \hat{\mathbf{n}} \tag{7}$$

where $\hat{\mathbf{n}}$ is the exterior unit normal to $\partial\Omega$. Some particular features of the system Eq.(5)-(7) merit comment: a) ψ is a complex quantity; b) the term $\nabla \times \nabla \times \mathbf{A}$ introduces cross derivatives of the form $\partial_{xy}A_i$; c) for a uniform field ($\mathbf{H_e} = constant$) the system is driven only through the boundary; and d) the simple form of the natural BC on ψ results from the gauge choice for $\mathbf{A}$ on $\partial\Omega$. Any other gauge choice results in a BC that also includes terms of the form $\psi\mathbf{A} \cdot \hat{\mathbf{n}}$.

Another TDGL model applicable to gapless superconductors with paramagnetic impurities and based on slightly different microscopic assumptions was proposed by Hu and Thompson [21]. This model further extended the ideas of Gor'kov, Elihasberg [11] and Schmid [10]. The scaled version of the corresponding equations then has the form [26], [30], [31].

$$\frac{\partial \psi}{\partial t} = \frac{1}{12}\left[-\left(-i\nabla - \mathbf{A}\right)^2 \psi - |\psi|^2\psi + \psi\right] \tag{8}$$

$$\frac{\partial \mathbf{A}}{\partial t} = -\frac{i}{2}(\psi^*\nabla\psi - \psi\nabla\psi^*) - |\psi|^2\mathbf{A} - \kappa^2\,\nabla \times \nabla \times \mathbf{A} + \nabla \times \bar{\mathbf{H}}_\mathbf{e} \tag{9}$$

with the same boundary conditions as in Eq.(7). A formal detailed comparison study of the models (5)-(6) and (8)-(9) is not the purpose of the present work. The latter model is introduced in one of the numerical studies to show that the sensitivity of the results to the mesh is not unique to the first model, but is of more general concern.

To elucidate the dependence of the nonlinear solution on the mesh we also consider a simpler model that has been more extensively analyzed. This simpler model and related results are discussed in detail in Section 5.

In the next section we briefly describe the numerical schemes used in the subsequent experiments.

3 Numerical Approximation

We are particularly interested in vortex formation, entry and pattern evolution to the steady state, and nonuniqueness implications for solutions on a given discretization mesh. Accordingly, we have developed a hybrid time-integration approach that can produce time accurate transient solutions or stable, lower order time step schemes that permit more rapid acceleration of the computation of the steady state problem. We have used two different software packages in the numerical studies, and verified them on a suite of test problems to ensure that the algorithms and implementation in both packages yield the same results.

Our basic numerical approach is to discretize the PDE systems in space, and to integrate the resulting semidiscrete system from specified initial data. In the 2-dimensional formulation, a mathematical transformation is used to map the equations from the physical coordinate system to a reference system in which the finite difference discretization is performed. This makes it possible for our simulator to accommodate more general physical domains with curvilinear, graded meshes that are still topologically structured. This feature is useful for application problems and situations in which local grading of the mesh (such as near an interior vortex) is of interest. The spatial discretization of the mapped equations on the reference domain is performed using a standard 9-point finite difference stencil. Another discretization approach based on finite elements in the physical domain is also being developed, but the particular choice of discretization scheme (finite difference, finite element or finite volume) is immaterial to the present work. The grid resolution is, however, a critical point of general interest.

The spatial discretization of the PDE in the 2D explicit simulations described later is implemented using a simplified "dial-an-operator" strategy in our research code FDTRANS. The nodal values of the computed quantities and all their derivatives through second order are made available via a user interface. This approach makes it easy to implement different physical models, since the user can construct nodal approximations for any desired PDE system (up to second order) using the given solution values and their derivatives. All spatial derivatives are discretized to second order accuracy in the reference domain, and the transformation metrics are also discretized to the same accuracy.

Numerical experience has shown that accurate discretization of the boundary conditions is very important for this application class. With the gauge choice discussed in the previous section, the boundary conditions become:

$$\frac{\partial \psi_r}{\partial \hat{\mathbf{n}}} = \frac{\partial \psi_i}{\partial \hat{\mathbf{n}}} = 0, \quad \mathbf{A} \cdot \hat{\mathbf{n}} = 0, \quad (\nabla \times \mathbf{A}) \times \hat{\mathbf{n}} = \mathbf{H_e} \times \hat{\mathbf{n}} \tag{10}$$

Here ψ_r and ψ_i respectively denote the real and imaginary components of the order parameter ψ. In our FDTRANS implementation, derivatives in the boundary conditions are discretized to second order accuracy using non-symmetric (one-sided) stencils. However, the edge and corner nodes require special treatment for implementing the conditions on $\mathbf{A}$, since the normal direction is not uniquely defined. To illustrate our approach in 2D, consider the lower-left corner (x,y)=(0,0) of a unit domain. The two sides of the domain that meet at this corner are the y-axis which we denote S1, and the x-axis denoted by S2. If we denote $\mathbf{A} = [a, b]^T$, the condition $\mathbf{A} \cdot \hat{\mathbf{n}} = 0$ implies $a = 0$ on S1 and $b = 0$ on S2. Using this in the

other condition for $\mathbf{A}$ yields

$$\frac{\partial b}{\partial x} = H_z \text{ on } S1, \quad \text{and } \frac{\partial a}{\partial y} = -H_z \text{ on } S2, \tag{11}$$

where H_z is the z-component of the applied field $\mathbf{H_e}$. At the corner we define the normal to be the average of that on S1 and S2, so the outward unit normal becomes: $\hat{\mathbf{n}} = \frac{-\hat{i}-\hat{j}}{\sqrt{2}}$, where $\hat{i}$, $\hat{j}$ denote the unit normal vectors in the $x-$, $y-$ directions respectively. If we use this definition of the normal, the two conditions given above for $\mathbf{A}$ reduce to the following at the corner node:

$$a + b = 0 \quad \text{and } \frac{\partial b}{\partial x} - \frac{\partial a}{\partial y} = H_z \tag{12}$$

Next we introduce one-sided (second order) difference approximations for $\frac{\partial b}{\partial x}$ (along S2) and for $\frac{\partial a}{\partial y}$ (along S1), and we use the fact that $a = 0$ on S1 and $b = 0$ on S2. The two boundary conditions then reduce to a 2×2 linear system which can be solved for a and b. This results in the following conditions at the corner:

$$a = \frac{2}{3}\frac{\Delta x \Delta y}{\Delta x + \Delta y} H_z, \quad b = -\frac{2}{3}\frac{\Delta x \Delta y}{\Delta x + \Delta y} H_z \tag{13}$$

Here we have assumed a uniform mesh with spacing Δx, Δy in the respective directions. A similar strategy can be used at the other corners. To summarize, we get

$$(a, b) = \rho \{(1, -1), (1, 1), (-1, 1), (-1, -1)\} \tag{14}$$

with

$$\rho = \frac{2}{3} H_z \Delta x \Delta y / (\Delta x + \Delta y) \tag{15}$$

for the corner values beginning at the bottom-left corner and proceeding in counter-clockwise direction.

Another strategy that we also considered for the corner nodes was to simply set $a = b = 0$, which seems reasonable since the two sides that intersect at each corner enforce $a = 0$ or $b = 0$ on the other boundary nodes. We remark that these are also the conditions recovered from the above expressions in the asymptotic limit as Δx, Δy approach 0. However, numerical experience shows that these simpler conditions do not work as well on practical meshes, and may impact the number of vortices as well as their behavior.

The spatial discretization step yields an ODE system which is integrated in time with a class of Runge-Kutta schemes. To illustrate the integration strategy, consider the semidiscrete ODE system obtained by spatial discretization of the TDGL models described in Section 2. The semidiscrete system can be written in the general form $\frac{d\boldsymbol{u}}{dt} = \boldsymbol{F}(\boldsymbol{u})$ where $\mathbf{u}(t)$ is the solution vector of grid point unknowns. Integrating through one step Δt_n from $\mathbf{u}(t_n)$ to $\mathbf{u}(t_n + \Delta t_n)$, the Runge-Kutta schemes that we utilize can be written in the following general form [32]

$$\mathbf{u}^{n+1} = \mathbf{u}^n + \Delta t \sum_{i=1}^{q} b_i \mathbf{k}_i \tag{16}$$

where the number of stages q, the value of the coefficients b_i, and the form of the functions $\mathbf{k}_i$ depend upon the specific scheme under consideration. Both explicit and implicit RK

schemes can be accommodated in the above formulation. For example, in the case of explicit schemes the functions $\mathbf{k}_i$ have the form

$$\mathbf{k}_i = \mathbf{F}(\mathbf{u}^n + \Delta t \sum_{j=1}^{i-1} a_{ij}\mathbf{k}_j) \tag{17}$$

where the coefficients a_{ij} constitute a strictly lower triangular $q \times q$ matrix whose entries depend upon the specific integration scheme. Since the scheme is explicit, each $\mathbf{k}_i$ depends only upon the previously computed stages.

Explicit integration methods described by Eq.(17) are of special interest for parallel solution, which is important for this application class due to the mesh resolution requirements, and is used in simulations on PC clusters for our high resolution grid studies (as we shall see later). Multistage explicit Runge-Kutta schemes are usually constructed to maximize the order of accuracy for a given number of stages. Such schemes typically have relatively small domains of stability. However, it is possible to construct alternative schemes that are of lower order accuracy but with larger stability regions permitting larger timesteps with the same number of stages. This can be quite effective for time accurate solution of moderately stiff problems when it is combined with an adaptive timestepping strategy. However, this type of approach may also be used to accelerate the convergence of time-stepping schemes to steady-state even in the case where the solution is no longer required to maintain time accuracy. In this latter case, one may even violate the stability restriction occasionally during the procedure since the timestepping algorithm functions essentially as an iterative method with each successive timestep solution now corresponding to an "iterate." Of course, this latter strategy is not time accurate, so the intermediate iterates no longer have any relation to the true time evolution of the solution. Moreover, one can adapt the choice of parameters as the solution evolves to meet the needs of the simulation goal. More specifically, q-stage schemes such as Eq.(16) and Eq.(17) can be constructed to exhibit different accuracy and stability properties by choosing different values for the coefficients b_i and a_{ij}. For example, the following coefficient values define a common 4-stage, fourth order accurate scheme

$$\begin{aligned} &a_{21} = a_{32} = 0.5, a_{43} = 1, a_{ij} = 0 \quad \text{for all other } i, j \\ &b_1 = b_4 = 1/6, b_2 = b_3 = 1/3 \end{aligned} \tag{18}$$

It can be shown through linear stability analysis for the standard model problem that this scheme is stable for $|\mu\Delta t| < 2.78$ where μ is the largest eigenvalue of the ODE system (here we assume μ to be real for simplicity). On the other hand, coefficient values for another 4-stage scheme which is only first order accurate are [33]

$$\begin{aligned} &a_{21} = 0.0156, a_{32} = 0.05, a_{43} = 0.1562, a_{ij} = 0 \quad \text{for all other} \quad i, j \\ &b_1 = b_2 = b_3 = 0, b_4 = 1 \end{aligned} \tag{19}$$

This scheme can be shown to be stable for $|\mu\Delta t| < 32$ (again μ is assumed to be real). The per-step cost of using the schemes Eq.(18) and Eq.(19) is the same, since each involves the same number of stages and function evaluations. Thus, the total cost of a simulation would depend upon the total number of steps required by each scheme. In general, when stiffness is not a significant factor and step-size selection is based on a specified accuracy

requirement one would expect the higher order method to yield higher computational efficiency. Depending on the severity of stiffness, however, the lower order method may perform more efficiently, particularly if it is more stable or costs less per step. This is because, as stiffness increases, step-size selection may become dominated by stability constraints rather than accuracy requirements. In the numerical studies described in Section 4, we compare these 4-stage schemes and present several simulation cases where the lower order explicit method performs significantly better due to its greater stability.

The 3D simulations, utilize the PEPPER3 [34] semiconductor process modeling software. The PDEs are again discretized in space to obtain a semidiscrete ODE system in time. In this instance, a seven-point FD stencil for the Laplacian is used with corresponding discretizations for the mixed partial derivatives. PEPPER3 calls the system integrator CVODE, a variable-step, variable-order integrator which uses either a Backward Differentiation Formula (BDF) or Adams method. These strategies follow the linear multistep formula,

$$\sum_{i=0}^{K_1} \alpha_{n,i}\ \boldsymbol{u}^{n-i}\ +\ \Delta t_n\ \sum_{i=0}^{K_2} \beta_{n,i} \boldsymbol{F}(\boldsymbol{u}^{n-i}) = 0 \tag{20}$$

where Δt_n is the stepsize, $\alpha_{n,0} = -1$, and the coefficients are chosen such that the formulas are exact for a polynomial of degree q. The Adams-Moulton formula uses $K_1 = 1$, $K_2 = q$, and is particularly effective on nonstiff problems. BDF methods follow by taking $K_1 = q, K_2 = 0$. For both integration schemes, the resulting algebraic system is solved using a quasi-Newton iteration. This increases the work per time step as compared to a fixed-point iteration, but for stiff problems this is offset by the better convergence properties enjoyed by Newton's method. A GMRES scheme is used to solve the linearized problem. The predictor-corrector integration strategy selects both the order of the method and stepsize to control the vector of estimated local error $\boldsymbol{e} = \boldsymbol{u}_{true} - \boldsymbol{u}$, so that $((1/N)\sum_{i=1}^{N} (\boldsymbol{e}_i/[\rho|\boldsymbol{u}_i| + \alpha])^2)^{1/2} \leq 1$, where ρ and α are relative and absolute tolerances, respectively.

4 Results and Discussion

The following numerical studies show that the discretized TDGL equations exhibit certain distinctive numerical effects associated with the mesh resolution, physical domain size and characteristic length scales, nonlinear behavior and hysteresis effects. For the 2D studies described below $\mathbf{H_e} = H_e \mathbf{e_z}$ with H_e constant. The domain is discretized with a uniform rectangular mesh of equal spacing in both directions. Unless otherwise indicated, we use $\kappa = 2$ in all the cases, and $\mathbf{A} = \mathbf{0}$ in Ω at $t = 0$.

The early transient behavior was first examined for the boundary conditions introduced in Section 2. We considered several cases with different initial data for ψ including random data. In all cases, the approximate solution evolves rapidly (within $2 \simeq 5$ time units) to a form where $|\psi| \sim 1$ throughout the domain and no vortices are present. Hence, for the time accurate solutions, to replicate our results one may take a randomized field ψ with $|\psi| = 1$ (e.g., $Re(\psi)$ random, and $Im(\psi) = (1 - Re^2(\psi))^{1/2}$). In the following numerical results, the vortices are displayed by plotting the magnitude of ψ over the simulation domain. As seen in the plot sequences for the time accurate solution, vortices enter the domain at the boundary and slowly move into the interior, pushed by the Lorentz-like force from the

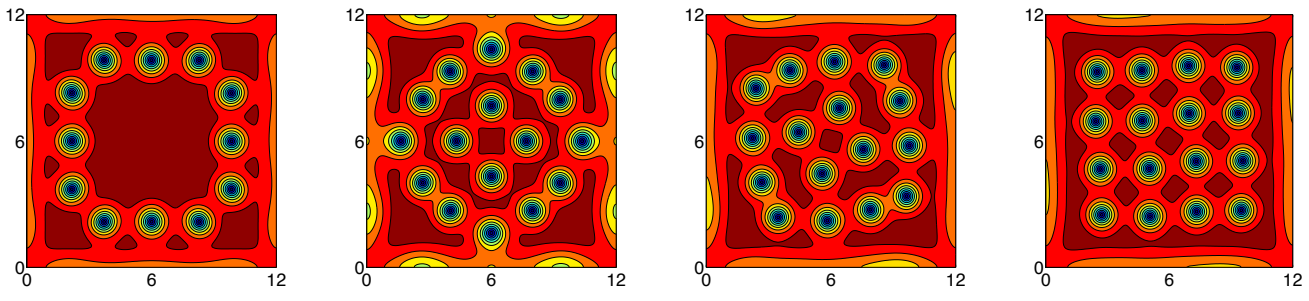

Figure 1: Contour plots of $|\psi|$ from Eq.(5)-(7) at different times for square domain of side-length 12 physical units with $\kappa = 2$ and $H_e = 0.95 = 0.475 H_{c2}$. The mesh contains 256×256 uniformly spaced nodes. The times are **(a)** $t = 20$, **(b)** $t = 80$, **(c)** $t = 350$ and , **(d)** $t = 1000$.

Meissner current. Eventually they form a stationary pattern in the interior, which is then sustained indefinitely. Figure 1 shows this evolution for a representative problem on a square domain of size $24\xi \times 24\xi$ and applied field $H_e = 0.95$. In our scaling $\lambda = 1$, so with $\kappa = 2$ this domain corresponds to a square of size 12×12 in scaled units, and the applied field translates to $H_e = 0.475 H_{c2}$. Note the symmetry of the vortex penetration at the earlier times shown in (a) and (b). This kind of transient configuration has been reported in the literature much more frequently than steady state results. The time taken for all the vortices to enter the domain is generally much shorter than the time needed by these vortices to rearrange and find a stable steady state configuration. For the time accurate regime we specify an absolute error tolerance of 10^{-5} in the 2D simulations with the RK scheme. It takes $t \simeq 80$ units of time to obtain the configuration in Figure 1 (b) but $t \simeq 1000$ is needed to get the vortex lattice in Figure 1 (d). Similarly, the result later in Figure 8 (a) is obtained after $t \simeq 50$ but one has to integrate up to $t \simeq 500$ to obtain Figure 8 (b). If the transient is not of interest, then one can accelerate the timestepping strategy as suggested earlier or employ other strategies such as the continuation scheme described later.

Here we show that inadequate mesh resolution may lead to spurious approximate solutions. Moreover, it may be very difficult to visually recognize that such an approximate solution is erroneous since it converges on the chosen mesh and may appear physically reasonable. We define a "spurious approximate solution" in the present context as one whose qualitative features are substantially different from the "correct" approximate solution obtained using much finer meshes for the same problem on the same computational domain.

In the first test case Eq.(7)-(9) is approximated on a $12\xi \times 12\xi$ domain with an applied field $H_e = 0.44 H_{c2}$. The scaling used in this system is based on $x \to \xi x'$ (instead of $x \to \lambda x'$ used in Eq.(5)-(7)). Thus, with $\lambda = 2$, $\kappa = 2$, the scaled length of each side of the domain is 12 units. Three uniform grids of size 32×32, 64×64, and 128×128 were used. The simulation was carried out with the same integration scheme and error tolerance, through $t = 500$ units of time. Figure 2 (a)-(c) show contour plots of the magnitude of the order parameter. For the 32×32 mesh, no vortex enters the domain, whereas for the 64×64 and

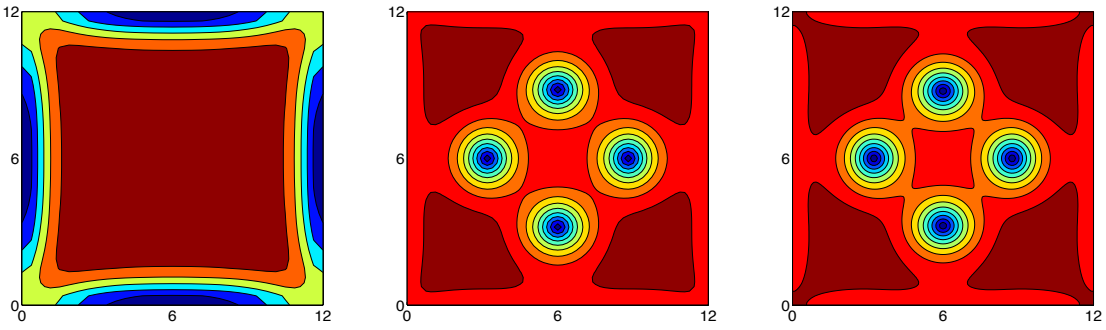

Figure 2: Magnitude of $|\psi|$ at $t = 500$ for the model given by Eq.(8)-(9) with $\kappa = 2$, $\bar{H}_e = 0.44 = 0.22 H_{c2}$ on a 12×12 domain with three different uniform meshes: (a) 32×32, (b) 64×64, and (c) 128×128. This illustrates the nature of the coarse grid spurious solution behavior.

128×128 mesh four vortices are seen!

For the second case, the problem Eq.(5)-(7) with $H_e = 0.95 = 0.475 H_{c2}$ is discretized on a $24\xi \times 24\xi$ domain with four grid densities: (a) 64×64, (b) 90×90, (c)128×128 and (d) 256×256 grid points. The results are shown in Figure 3 for simulations on these respective grids. For the coarsest grid (a), vortices penetrate the domain and start to redistribute normally. The fact that the mesh resolution is inadequate appears only later during the transient calculation: at $t \simeq 180$, the order parameter starts to exhibit extended regions of depletion ($|\psi| = 0$) which are non-physical. These regions increase at a very slow rate and Figure 3 (a) shows the result at $t = 400$. If the integration is continued, the trivial solution ($|\psi| = 0$) is approached everywhere. This artifact of poor mesh resolution disappears when the problem is recomputed on finer grids! This result on the coarsest mesh is a striking departure from the nontrivial solutions obtained on the finer grids as indicated in Figures 3 (b) - (d) where the integration has been carried out until the solution remains unchanged for $\sim 10^3$ units of time. The solution is changing very slowly, and for practical purposes a steady state has essentially been reached. Note that these nontrivial steady states also differ.

Hence, in the case of Figure 3 we find that, for a number of intermediate grid densities ranging from 90×90 to approximately 200×200, the stationary result is grid dependent: denser grids allow more vortices to penetrate and to rearrange in a more regular distribution than the coarser grids permit. The numerical results strongly suggest that the pattern shown in Figure 3 (d) is the correct answer because it remains unchanged under further mesh refinement for meshes between $\simeq 200 \times 200$ and 324×324. One may argue that, given the nature of the problem (symmetries in domain geometry and boundary conditions), the intermediate results (b) and (c) look suspicious. However, for a more general problem domain and boundary conditions, it will be very difficult to reject false numerical solutions or suspect their validity without further analysis or grid refinement studies. An error indicator analysis similar to those applied in adaptive mesh strategies would be useful [35]. Otherwise, as applied here, one must at least recompute on successively refined grids to verify whether a computed result is physically correct and that it yields the same configuration with the same

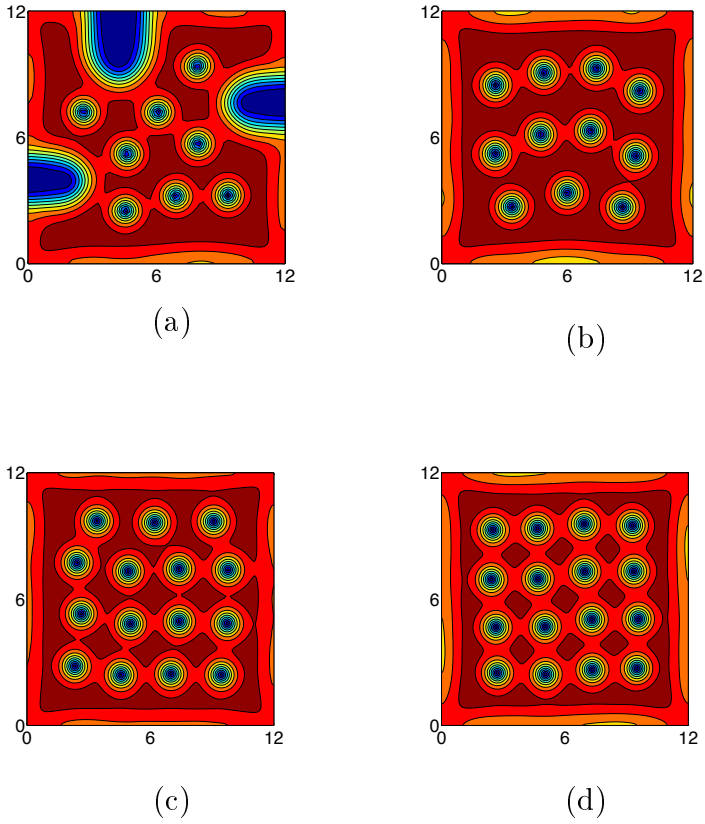

Figure 3: Magnitude of $|\psi|$ from from Eq.(5)-(7) for $H_e = 0.95 = 0.475 H_{c2}$ on a 12×12 domain. The meshes densities are **(a)** 64×64, **(b)** 90×90 **(c)** 128×128, **(d)** 256×256. The result in (a) is a snapshot at $t = 400$ indicating clearly a non-physical solution. The depleted regions become wider (very slowly) until the trivial solution $|\psi| = 0$ is obtained everywhere. (b)-(d) represent long-term invariant configurations (no change over several 10^2 units of time).

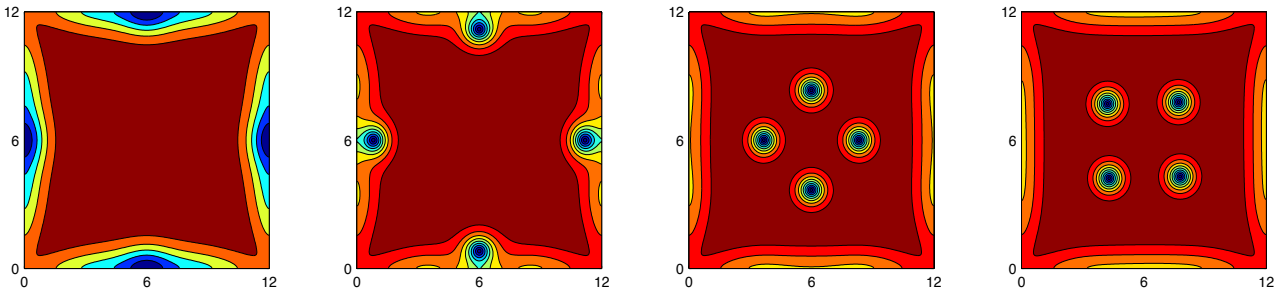

Figure 4: Magnitude of ψ for applied field $H_e = 0.80 = 0.40H_{c2}$ on 200×200 mesh at the following time instants: (a) t=60, (b) t=70, (c) t=200, and (d) t=4000.

number of vortices. In this case the difference in successive solutions is the error indicator and is, of course, more reliable than a residual or truncation error based estimate. This can also be augmented by Richardson extrapolation.

We would like to point out that we have carried out several very long term simulations in an effort to verify that the square lattice we see in Figure 3 (d) in fact represents the steady-state result. For example, we recomputed the results shown in Figure 3 (d) up to t=5000 and saw no change between t=1000 and t=5000. The square lattices in our steady-state results occur instead of the theoretical Abrikosov triangular lattices due to the the effects of the boundary and also the specifics of the problem domain size and applied field. We explore these points in greater detail next.

According to this theory, if the domain is infinite the lattice is triangular, but as we now show, the situation is far more complex than the known theoretical results suggest. In the finite domain case, domain size, applied field and boundary effects play a significant role in both the evolution of the vortex patterns and their final structure. We develop these ideas next with a series of supporting numerical investigations. We begin with the problem domain and model shown in Figure 3, but with varying applied field. Let us consider the situation when the applied field is incrementally increased from $H_e = 0.78 = 0.39H_{c2}$. For this and lower field values, the numerical results show that no vortices enter the domain. We performed these calculations using a 200×200 mesh. Next, H_e is increased incrementally and the calculations repeated from the same initial data and with 200×200 mesh. At $H_e = 0.80 = 0.40H_{c2}$ and $t \sim 60$, we see four vortices simultaneously begin to enter the domain at the mid-side locations (see Fig. 4 (a)), and have fully entered by $t \sim 70$ (see Fig. 4 (b)). They continue to move toward the center (Fig. 4 (c)) and then rotate into the steady-state square configuration in Figure 4 (d). Note that a square pattern, and not a triangular pattern, is obtained in the steady-state.

A series of similar calculations were made with applied field increased by increments through $H_e \sim 1.02 = 0.51h_{c2}$. For field values above $H_e \sim 0.87$ we also repeated the calculations with a mesh resolution of 300×300 to verify that we get the same number of vortices as on the 200×200 mesh. We find that in the range $H_e \sim 0.80 - 0.82$ four vortices enter the domain and evolve to a square pattern. The key difference is that as H_e increases,

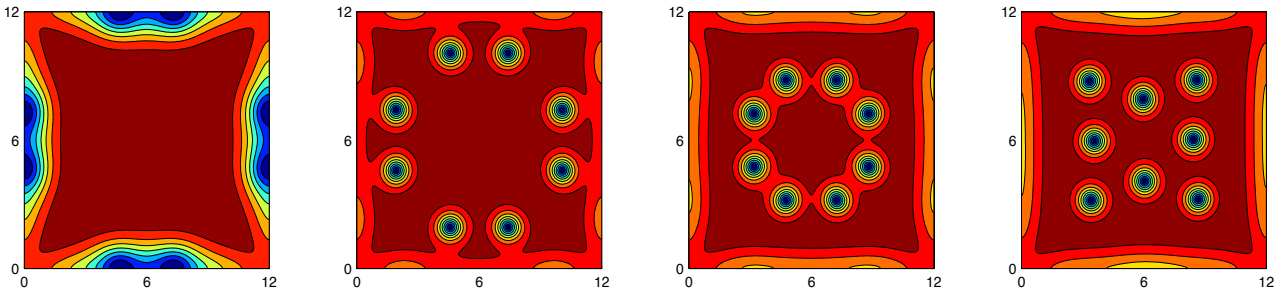

(a) (b) (c) (d)

Figure 5: $|\psi|$ with applied field increased to $H_e = 0.84 = 0.42H_{c2}$ on 200×200 mesh at: (a) t=20, (b) t=30, (c) t=200, and (d) t=4000.

the vortices enter the domain earlier; for example, at $H_e = 0.81$ they begin to enter by $t \sim 40$, and are fully inside the domain by $t \sim 50$. As the field value increases to $H_e \sim 0.82$ we see eight vortices enter the domain. For $H_e = 0.82$ they begin to enter at $t \sim 30$ in the form of pairs from the mid-sides of the domain. They then evolve into a pattern that is not a square (since 8 is not a perfect square). In this case, one can discern subgroups of triples that suggest a "triangular" lattice of sorts. Figure 5 shows this evolution sequence for the case $H_e = 0.84$. As we continue to increase the applied field, the basic behavior with the eight vortices follows that observed earlier for the four vortex case, until at $H_e \sim 0.88$ we find that an additional vortex begins to enter at each mid-side (behind the first pair) yielding twelve vortices. These twelve vortices evolve to a pattern that also resembles a "triangular" sort of structure (see Fig. 6). Similar 12-vortex solutions are seen for field values in the range $H_e \sim 0.88 - 0.93$, again the key difference being that larger field values cause the vortices to enter the domain at lower values of t. Figure 6 shows the 12-vortex evolution sequence for an applied field $H_e = 0.90$. Notice that we are now using a 300×300 mesh. Continuing this experiment, as H_e increases further we see 16 vortices enter the domain in the range $H_e \sim 0.94 - 0.99$. Since 16 is a perfect square, the vortex pattern in these cases does evolve to a square lattice in the long-term (see Fig. 3). If we continue to increase H_e, we see 20 vortices for $H_e \sim 1.0$, and they evolve to an irregular pattern, since 20 is not a perfect square.

In addition to the systematic experiment discussed above, we have also computed results for certain selected field values that are larger than $H_e = 1.02$ which are shown later. As expected, in these cases we see even larger number of vortices, and they evolve in ways similar to those seen in the preceding experiment. More comprehensive results and their detailed discussion is given in [36].

One of the key conclusions from this experiment is that the final configuration of the vortex pattern depends upon the number of vortices admitted into the domain. We have made an extensive literature study of computational results pertaining to this mesh sensitivity problem for GL simulations, and have found that the number of grid points per coherence length ξ or the grid density typically varies between 2 to 5 [26], [28], [30].

Other studies [29], [31], [37] failed to provide the information necessary to determine

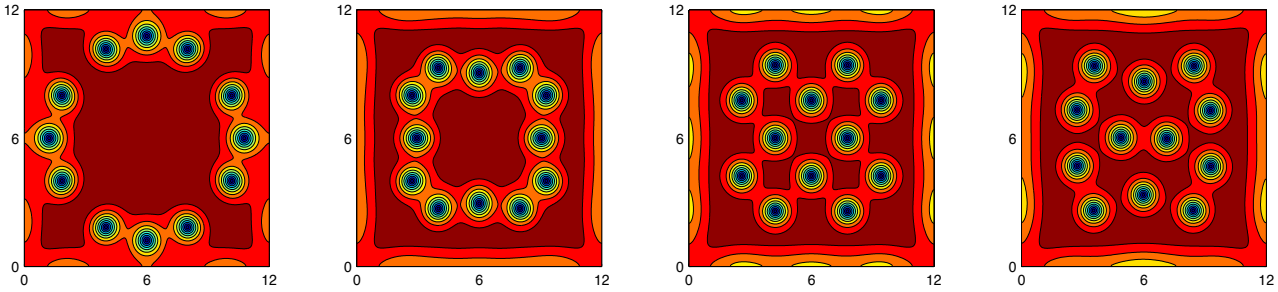

Figure 6: $|\psi|$ for applied field $H_e = 0.90 = 0.45H_{c2}$ on 300×300 mesh at: (a) t=20, (b) t=40, (c) t=400, and (d) t=4000.

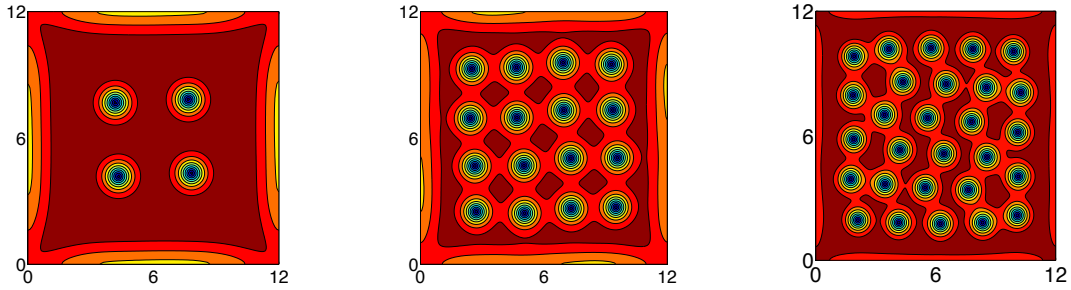

Figure 7: Vortex configurations from Eq.(5)-(6) with $\kappa = 2$, for three values of the external applied field: **(a)** $H_e = 0.80 = 0.40H_{c2}$, **(b)** $H_e = 0.95 = 0.475H_{c2}$ and **(c)** $H_e = 1.10 = 0.55H_{c2}$. The grids are 128×128, 200×200 and 304×304 respectively.

the grid density (either the mesh size or the physical domain size were not available) so presumably these are not felt to be important.

For our preceding simulation studies, the grid densities (i.e., nodes per coherence length) were 2.67 for Figure 2 (a) and Figure 3 (a), 5.33 for Figure 2 (b) and Figure 3 (c), 10.66 for Figure 2 (c) and Figure 3 (d), and as high as 12.66 for Figure 7 (c). Note that meshes with less than 7-10 grid points per ξ generate spurious results so it is reasonable to infer that results in the literature with this TDGL model are suspect, especially in the absence of a mesh refinement study. The required mesh density numbers vary with H_e; the higher the applied field, the greater the requirement for fine meshes becomes.

The mesh sensitivity behavior in this application is very different and more critical than that seen in many other application areas in engineering or science. Significantly, it is quite different from the mesh behavior observed in semiconductor simulation for microelectronic devices [38]. In device applications, poor resolution may lead to divergence and breakdown of the numerical algorithm. This is often the case in applications where mesh sensitivity stems from convective effects. However, in such cases, with the use of certain special stabilization

or upwind strategies, it is possible to realize at least a qualitatively correct solution even on coarse meshes. This may lead to an overly dissipative approximation but there is little risk of converging to a radically different solution of the type which was exhibited here. In the present application we have seen that spurious solutions are pervasive and often easy to mistake for the true solution. This would be particularly detrimental for the designer who would use the results of a numerical simulation to model the vortex dynamics and vortex pinning in a superconductive material [39]. Therefore, it is imperative that mesh refinement studies and reliability analysis be performed to confirm the validity of all numerical results.

As these studies also demonstrate, the applied field is a key factor affecting the structure of the vortices and their arrangement. As the magnitude of the field increases, the average separation between vortices decreases or the number vortices within a given simulation domain increases [40]. As also noted there, the mesh must be refined as the field is progressively increased and the mesh scaling with the field is not linear. Thus, whereas a 128×128 grid appears sufficient to accommodate the lower applied field $H_e = 0.80$, very fine grids like the 304×304 mesh are required for the large applied field $H_e = 1.1$. In addition, the bifurcation points at which the vortex pattern increases in number are not equally separated.

Next we consider the effect of domain size, since we have found that the number of vortices entering the domain is also a very strong function of its size. We repeated the previous experiment with a domain size of 16×16 scaled units (i.e., $32\xi \times 32\xi$ for our scaling), for certain selected values of applied field. For example, if we consider a field of $H_e = 0.90$ for this domain size, the number of vortices increases to 28 (from 12 for our previous case of a 12×12 domain). In addition, the mesh resolution required to obtain a valid solution becomes even finer. With the smaller domain we could use a 200×200 mesh, which corresponds to a spacing of 0.06 in each direction. This same spacing for the larger domain appears inadequate, and we have to use at least 300×300 nodes to get valid solutions.

The reason for this behavior is that on finite simulation domains, the arrangement of the vortices is influenced by the surface barrier effect. If the physical dimensions of the domain are of the order of a few coherence lengths e.g. $\simeq 10\xi$, then the vortex dynamics is strongly affected by the presence of the boundary. For example, at a higher field $H_e = 1.10$, there are four vortices in the $10\xi \times 10\xi$ domain and only one in the $8\xi \times 8\xi$ domain. For a lower field with $H_e = 0.88$ four vortices are present in a $12\xi \times 12\xi$ domain as seen in Figure 8, but there are no vortices in a smaller $10\xi \times 10\xi$ domain. Figure 8 shows that the four vortices which are present in the $12\xi \times 12\xi$ domain at $t = 160$ (a) start a rotation at around $t \simeq 300$ and end up in the locked configuration (b). This configuration is largely determined by the domain geometry and boundary proximity.

From these results it can be deduced that the number of vortices and their relative location depend upon both domain size and applied field. We emphasize this point because the influence of domain size apparently has not been explored in previous investigations. Simulations on large physical domains with fine resolution, through lengthy transients, would further impact computational resource needs and algorithm design.

In the previous simulations we have considered initial conditions for ψ that were either constant or randomized with the provision that $|\psi| = 1$. In such cases, the number of vortices that enter the domain for a given domain size and applied field, as well as their final

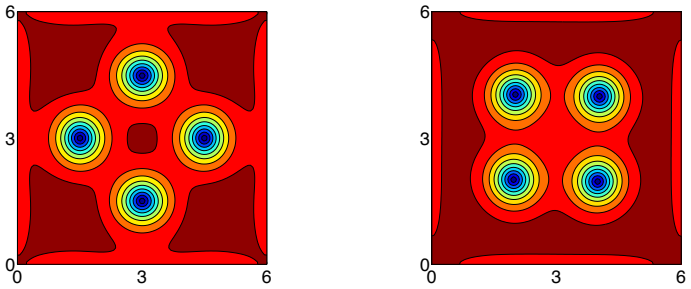

Figure 8: Contour plot of $|\psi|$ from the model Eq.(5)-(7) for $\kappa = 2$, $H_e = 0.88 = 0.44 H_{c2}$ on a $12\xi \times 12\xi$ domain at (a) $t = 160$ and (b) $t = 400$

geometric configuration, does not depend upon the precise choice of initial data. However, another series of studies revealed that the question of dependence on initial data is much more complicated. This is not surprising considering the results we show later for a simpler model in Section 5.

In the present study with the full model, we used the computed results from the previous experiments as initial data as we varied the applied field. For example, in Fig. 4 the applied field is $H_e = 0.80 = 0.40 H_{c2}$, and four vortices enter the domain (here we have used the simple initial conditions with $|\psi| = 1$). If we use this 4-vortex result as initial data and lower the value of applied field, we find that the vortices remain in the domain even for values of H_e far below the previous threshold value where the first set of vortices are seen. Similarly, when we use the 16-vortex result previously computed for $H_e = 0.88$ as initial data for field values as low as $H_e = 0.82$ (which previously yielded four vortices), we find that the 16 vortices persist and reach a steady-state square lattice as well.

These results, taken in conjunction with those in Section 5, strongly suggest that the full model very likely admits multiple solutions. We carried out several similar studies with varying initial conditions and repeatedly observed cases of nonuniqueness.

5 A Related Model

Our numerical investigations conclude with the study of a related simpler model that has been theoretically analyzed by Bethuel, Brezis, and Helein [41]. The model consists of the following complex-valued Ginzburg-Landau type of equation. Let Ω be a region in $\mathbb{R}^2$ with smooth boundary and consider solving

$$\begin{aligned} -\Delta \psi_\varepsilon &= \frac{1}{\varepsilon^2} \psi_\varepsilon (1 - |\psi_\varepsilon|^2) \qquad \text{in } \Omega, \\ \psi &= g \qquad \text{on } \partial\Omega \end{aligned} \tag{21}$$

where $g : \partial\Omega \to S^1$ is a given function mapping into the unit circle, and ϵ is a small parameter that approaches 0. If g has topological degree $\deg(g, \partial G) = d > 0$, then the

solution ψ_ε will exhibit exactly d vortices, of decreasing radius as $\varepsilon \to 0$. We exploit this property to study the discretization effect on the solution pattern and gain insight into the behavior of the more complex TDGL model. If Ω is starshaped, there is a subsequence $\varepsilon_n \to 0$, exactly d points $a_1, a_2, ..., a_n$ in Ω, and a smooth harmonic map $\psi_\star$ from $\Omega \setminus \{a_1, a_2, ..., a_n\}$ into S^1 with $\psi_\star = g$ on $\partial\Omega$, such that ψ_{ϵ_n} converges to $\psi_\star$. As stated in [41] it is essential to pass to a subsequence: in general ψ_ε is not unique and various subsequences converge to different limits. This reflects the non-uniqueness found in our numerical studies.

The local structure and location of the singularities $a_1, a_2, ..., a_n$ (vortices) is important from an application standpoint. Each vortex has degree $+1$ and there are complex constants α_i, $|\alpha_i| = 1$, such that

$$\left| \psi_\star(z) - \alpha_i \frac{z - a_i}{|z - a_i|} \right| \leq C|z - a_i|^2$$

as z approaches a_i. This gives structural information about the solution near the vortices. Although $\psi_\star$ has infinite energy, it is possible to define a renormalized energy W, which is finite.

$$W(a) = -\pi \sum_{i \neq j} \log|a_i - a_j| \; + \; \frac{1}{2} \int_{\partial G} \Phi_0 (g \times g_\tau) - \pi \sum_{i=1}^{d} R_0(a_i)$$

where $\Phi_0(x)$ solves $\Delta\Phi_0 = \sum_{i=1}^{d} 2\pi\delta_{a_i}$ with Neumann boundary conditions $\dfrac{d\Phi_0}{d\nu} = g \times g_\tau$, $\int_{\partial G} \Phi_0 = 0$, and $R_0(x) = \Phi_0(x) - \sum_{j=1}^{d} \log|x - a_j|$. The solution $\psi_\star$ is a minimizer for W; moreover, $W \to \infty$ as two of the vortices coalesce, or as one of the vortices approaches ∂G.

In our numerical study we take Ω to be square $[-.5, .5] \times [-.5, .5]$ and $g = \cos(w\theta) + i\sin(w\theta)$. Here w is the integer winding number and $0 \leq \theta \leq 2\pi$ is the angular coordinate along $\partial\Omega$. From the analysis of Bethuel et. al., it follows that $|\psi|$ should contain w vortices.

Numerical studies were carried out for winding numbers 1 through 20; the results confirm the expected number of vortices in each case. Figure 9 shows results for selected values of w, on a 100×100 uniform mesh with $\varepsilon^2 = 0.001$. However, the studies also reveal several interesting features that are worth noting because they also occur to varying degrees in the full Ginzburg-Landau model.

Nonlinear convergence is difficult to attain for many values of the winding number w. Incremental continuation in ε is helpful for certain values of w, but fails for others. In the successful cases, we used this strategy in conjunction with a constant initial guess for ψ. On the other hand, continuation in w, at the fixed final value of ε, appears to be more effective for attaining convergence. It is difficult to solve the linear systems that arise within the nonlinear iterations using the usual preconditioned Krylov subspace methods for several cases. We found it cheaper in many cases to use a direct solver instead of ILU preconditioned GMRES.

For some values of w, the solution is clearly not unique: there are multiple limit functions ψ_ε, each having the same number of vortices, with different geometric configurations. See the results obtained with different initial guesses for $w = 17$ in Figure 10. We saw similar instances of nonuniqueness for several other values of w as well.

The presence of multiple solutions and dependence of vortex patterns on the mesh support the previous observations on the more complex TDGL model.

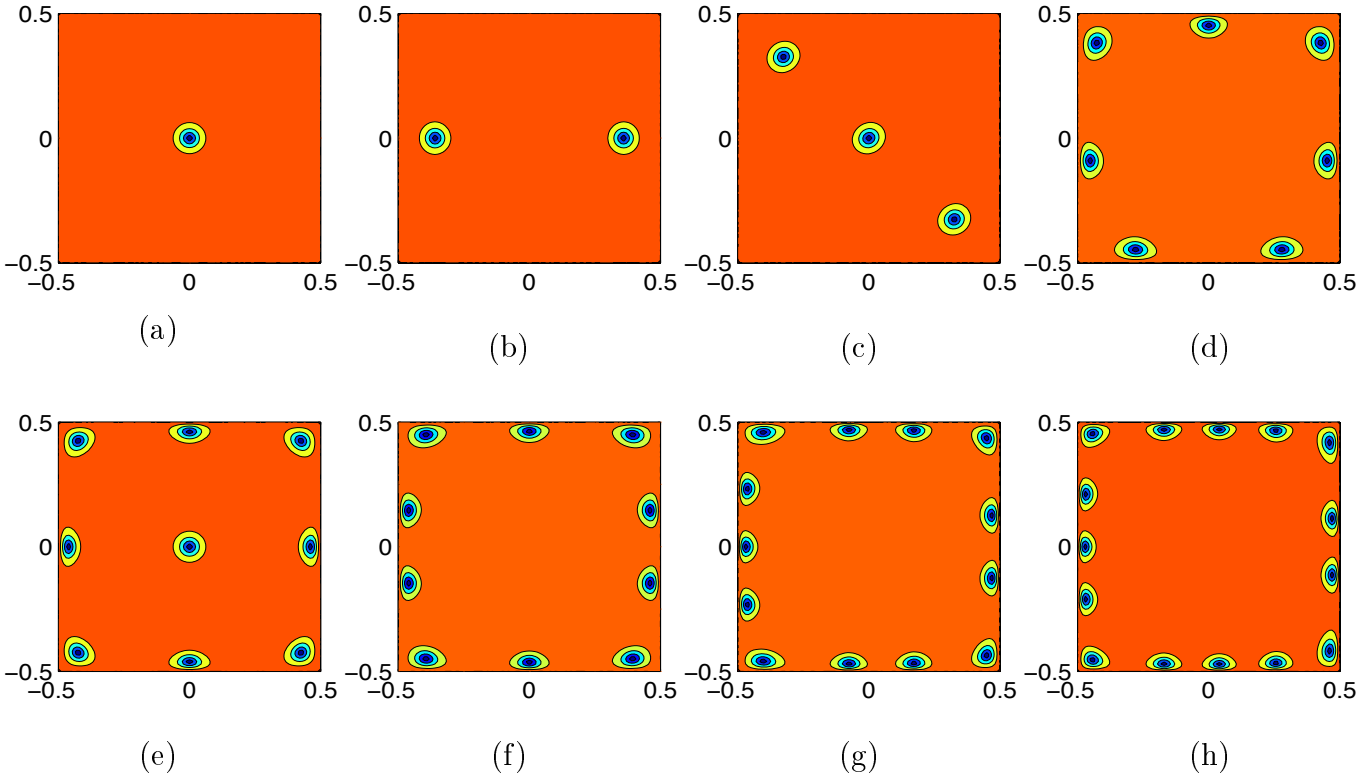

Figure 9: Steady-state vortex patterns in the solution $|\psi|$ of equation (21) with $\epsilon^2 = 0.001$ on a 100×100 uniform mesh with different winding numbers: (a) $w = 1$, (b) $w = 2$, (c) $w = 3$, (d) $w = 7$, (e) $w = 9$, (f) $w = 10$, (g) $w = 13$ and (h) $w = 15$.

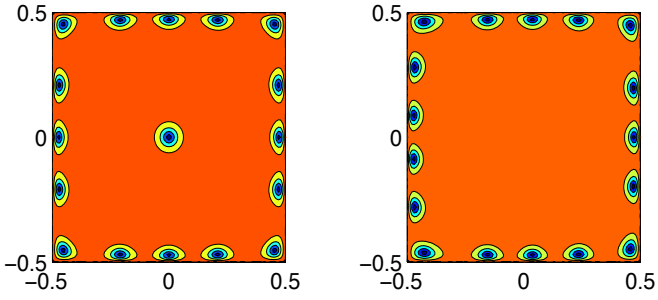

Figure 10: Steady-state solutions of (21) for winding number $w = 17$ on a 100×100 uniform mesh with $\epsilon^2 = 0.001$ using different initial guesses.

6 Algorithm performance

As expected stiffness becomes increasingly significant as the mesh resolution becomes finer. The discretized diffusion operator contributes to the stiffness and so do some of the other terms, which have strong nonlinearities and involve cross-derivatives. Numerical experience confirms the expected increase of stiffness as the mesh is refined. This is seen in the form of decreasing integration step sizes and reduced effectiveness of adaptive step-size control algorithms. In our simulator FDTRANS, the step-size control algorithm keeps track of the number of "rejected steps," and this number increases (relative to the total number of steps) as stiffness increases.

Numerical results that compare the performance of the 4-stage, 4-th order and the 4-stage, 1-st order Runge-Kutta schemes are given in Table 1. In all the test cases we specify a fixed temporal error tolerance, which the integration algorithm satisfies at each step by adaptively selecting the step-size. Here we consider again the square domain of size 24ξ, with $H_e = 0.88$ and with a specified time truncation error tolerance of 10^{-5}. The three rows in the table correspond to different grid resolutions but not the same problem. The 1st order scheme performs better than the 4th order scheme in all cases, mainly because of the improved stability of this particular 1st order scheme, which can use much larger step-sizes for these stiff problems.

mesh	order	CPU time (sec.)	# of steps	% rejected steps
64×64	4th order	2730.77	16548	30.79
	1st order	411.51	2254	46.49
200×200	4th order	20672.75	105592	22.85
	1st order	5468.21	35096	17.49
256×256	4th order	47892.98	168784	28.03
	1st order	12167.23	51776	20.43

Table 1: Performance comparison of 1st and 4th order integration methods for representative problem on domain of 24×24 scaled length units with different choices of mesh resolution.

Various continuation schemes can be introduced to accelerate convergence of the algorithm to the steady state. For example, one can elect to apply incremental continuation in a parameter, modify the coefficients in the time-dependent term, or modify the boundary conditions. We have explored continuation in the boundary conditions to accelerate "arrival" to the steady-state, and show representative results for the 3D problem.

Assume that the steady state solution is to be computed with a mixed condition such as $B(u) \equiv \mu \partial u/\partial n + \nu u - \gamma = 0$. In the present work this is implemented by considering the least-squares functional $\phi(u) = \eta \frac{1}{2} \|B(u)\|^2$ and the associated ODE $dz/dt = -\nabla \phi(z(t))$, describing the path of steepest descent. Here η is a factor that determines the weight given to enforcing the boundary condition relative to satisfying the PDE system. This can be done in the function space setting ($H^{-\frac{1}{2}}$) or in the semidiscrete setting where it gives rise to another differential equation for each boundary point, and is a convenient continuation process for gradually enforcing the boundary conditions throughout the integration, instead of forcing them to be satisfied at every timestep. This gives a first-order ODE at boundary

nodes for the components of $\mathbf{A}$, which is much more amenable to the multistep integration strategy than algebraically enforcing the flux BC's.

In the tests described here, meshes are uniform in each direction and the error control is based on the above criteria, with relative tolerance $\rho = 10^{-2}$ and absolute tolerance $\alpha = 10^{-5}$. Table 2 compares the Adams and BDF integration strategies for TDGL on a sequence of meshes. The physical parameters are $\kappa = 2$, $t = 100$, $\mathbf{H_e} = (0.1, 0.1, 1)$, and $\Omega = 6.67 \times 6.67 \times 3.34$ in λ units. In all cases the Adams method was between two to three times faster than BDF. Moreover, the order for the Adams scheme started at 1, increased to 3, and then settled down to 2 for most of the integration, whereas BDF used primarily first order. If the tolerances were to be reduced significantly, BDF should compare more favorably with Adams.

		CPU	Steps	NCF
$20 \times 20 \times 10$ mesh	Adams	214	609	7
	BDF	640	1023	283
$30 \times 30 \times 15$ mesh	Adams	860	1029	13
	BDF	2367	1638	469
$40 \times 40 \times 20$ mesh	Adams	6050	2105	10
	BDF	14435	2437	670

Table 2: Comparison of Adams versus BDF integration schemes in 3D. NCF is the number of nonlinear convergence failures. Adams is much more effecient for the given tolerances.

The left panel of Figure 11 shows the steady state results with $\kappa = 2$, a mesh of $50 \times 50 \times 25$, and $\mathbf{H_e} = (0.3, 0.3, 1)$. Isosurfaces $|\psi| = 0.3$ are plotted at $t = 100$. Eight well-defined vortices with slight tilts due to $\mathbf{H_e} \neq \boldsymbol{e}_3$ are evident. The right panel of Figure 11 shows the results with $\mathbf{H_e} = (0.6, 0.6, 1)$. The tilt becomes much more extreme, so that the vortices leave the domain through its sides rather than the top. A finer mesh in the z-direction is necessary to properly resolve the normal intersection of the vortex axis with the side wall.

As mesh resolution is increased, the stiffness of the ODE system increases, causing an exponential increase in cpu time. For $t = 50$, $\mathbf{H_e} = (0.6, 0.6, 1)$, and grid $80 \times 80 \times 40$, the Adams method required 15169 time steps and took 315,365 cpu seconds on a 500 MHZ processor. There are several approaches to alleviate this performance degradation. One could employ a multigrid strategy for the linear solver. More generally, various preconditioners could be tried within the CVODE framework. For example, Sobolev gradient preconditioning within a descent algorithm has been successfully applied to the 2D stationary problem [43].

As regards the sensitivity of the approximate solution to the mesh resolution, results similar to those described above for the 2D problem were also obtained here. As the mesh is refined from $30 \times 30 \times 25$ to $50 \times 50 \times 25$, the number of vortices that the mesh can support increases from four to eight.

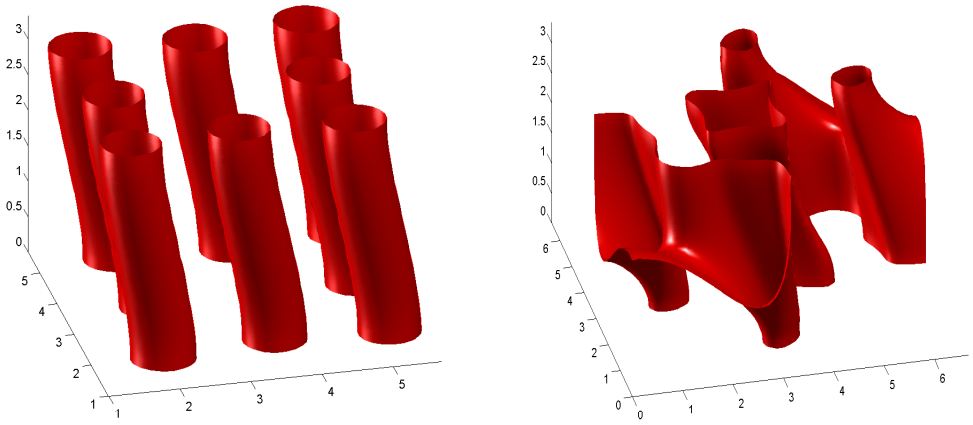

Figure 11: Vortex filaments in 3D with physical parameters $\kappa = 2$, $t = 100$, and $\Omega = 6.67 \times 6.67 \times 3.34$ in λ units. In the left panel the external field is $\mathbf{H_e} = (0.3, 0.3, 1) = (0.15, 0.15, 0.5)H_{c2}$, while in the right panel $\mathbf{H_e} = (0.6, 0.6, 1) = (0.3, 0.3, 0.5)H_{c2}$.

7 Concluding Remarks

Our numerical studies for transient and steady state solution of the time-dependent Ginzburg-Landau model for superconductivity reveal several interesting issues. Foremost among these is mesh sensitivity and the distinctive ways in which it is manifest. Another key conclusion from our studies is the presence of non-unique solution states, which we have conclusively demonstrated for the simple model.

Our results show that inadequate mesh resolution often causes the numerical results to exhibit spurious, non-physical solutions and effects similar to hysteresis in the number of vortices if the field is increased and then decreased. Furthermore, in many cases such solutions appear physically very reasonable, which makes it easy to mistake them for a valid solution. This would be particularly true on domains of irregular shape or with boundary conditions that are less symmetric. Thus, it is important to validate any simulation result for this problem class by recomputing it on finer meshes until its features remain invariant with respect to mesh density and through the use of reliable computed error indicators.

The need for sufficient spatial resolution to insure an accurate solution is consistent with theoretical analyses of the simpler model by Bethuel, Brezis, and Helein. Here the number of vortices formed is related to the winding number of the boundary function g. Our simulations with this model confirm and reinforce the effect of mesh resolution on the number of vortices. In addition, we have shown that simulations with a fixed winding number and mesh may lead to different steady-state solutions even while the number of vortices remains the same. This clearly shows the problem admits multiple solutions. The presence of nonunique solutions may partly explain the hysteresis effects observed for the full model.

Another issue is that the domain size necessary to realize the essential solution features must exceed a minimal number of characteristic lengths. This fact, coupled with the relatively fine resolution needed and the large number of vortices that may arise, implies that meshes with very large number of nodes are often required.

Exploratory three dimensional studies have also been presented which show that the

mesh issues we see in 2D become even more critical in 3D and this causes computational efficiency to become a paramount concern.

Finally, we remark that, in addition to algorithmic improvements that lead to higher efficiency, we are also exploring distributed parallel implementation on computer clusters to gain speedup in simulation time. Preliminary work in 2D has been very promising, and we plan to extend these ideas to 3D.

References

[1] Proceedings of the Fourth Symposium on Low Temperature Electronics and High Temperature Superconductivity / Symposium on Low Temperature Electronics and High Temperature Superconductivity (4th : 1997 : Montreal, Quebec) / Pennington, NJ / 1997.

[2] Proceedings of EUCAS 1997, The Third European Conference on Applied Superconductivity held in the Neth / European Conference on Applied Superconductivity (3rd : 1997 : Veldhoven, Netherlands) / Bristol / 1997.

[3] Proceedings of the 1999 University of Miami Conference on High Temperature Superconductivity, Coral Gables, January 7-13,1999 - Woodbury, N.Y. : American Institute of Physics, (1999).

[4] T. Van Duzer and C. W. Turner, Superconductive Devices and Circuits, Prentice Hall PTR, Upper Saddle River, New Jersey, 1999, ISBN 0-13-262742-6.

[5] T.P.Orlando, K.A.Delin, *Foundations of Applied Superconductivity*, (Addison-Wesley,1991).

[6] Proceedings of the 6th International Conference on Materials and High Temperature Superconductivity, Feb. 20-25 2000, Houston, Texas (2000) : to be published.

[7] J. W. Neuberger, *Sobolev Gradients and Differential Equations*, (Springer V., 1997).

[8] A.A.Lorber, G.F.Carey, W.D.Joubert, ODE Recursions and Iterative Solvers for Linear Equations, *SIAM J. Sci. Comput.* **17**, 1, p.65 (1996).

[9] A.A.Lorber, G.F.Carey, S.W.Bova, C.Harle, Accelerated Solution of Non-Linear Flow Problems Using Chebyshev Iteration Polynomial-Based Runge-Kutta Recursions, *Comp. and Fluids*, **27**, 7, p.769 (1998).

[10] A. Schmid, A time-dependent Ginzburg-Landau Equation and its application to the problem of resistivity in the mixed state, *Phys. Kondens Matter.* **5**, p.302 (1966).

[11] L. P. Gor'kov, G. M. Eliashberg, Generalization of the Ginzburg-Landau equations for non-stationnary problems in the case of alloys with paramagnetic impurities, *Sov. Phys. JETP* **27**, 2, p.328 (1968).

[12] V.L.Ginzburg, L.D.Landau, *J. Exptl. Theoret. Phys.* (USSR), **20**, p.1064 (1950).

[13] A. A. Abrikosov, *Soviet Phys. - JETP.* **5**, p.1174 (1957).

[14] L. P. Gor'kov, Microscopic Derivation of the Ginzburg-Landau equations in the theory of superconductivity, *Soviet Physics - JETP* **9**, 6, p.1364 (1959).

[15] J. Bardeen, L N. Cooper, J. R. Schrieffer, *Phys. Rev.* **108**, p.1175 (1957).

[16] M. J. Stephen, H. Suhl, Weak Time Dependence in Pure Superconductors, *Phys. Rev. Lett.* **13**, 26, p.797 (1964).

[17] P. W. Anderson, N. R. Werthamer, J. M. Luttinger, An Additional Equation in the Phenomenology of Superconductivity: Resistive Effects, *Phys. Rev.*, **138**, 4A, p.1157 (1965).

[18] E. Jakemin, E. R. Pike, Time-Dependent Ginsburg-Landau Theory, *Phys. Lett.*, **20**, 6, p.593 (1966).

[19] L. P. Gor'kov, On the Energy Spectrum of Superconductors, *Soviet Phys. JETP*, **34**, 3, p.505 (1958).

[20] A. A. Abrikosov, L. P. Gork'ov, I. E. Dzyaloshinski, *Methods of Quantum Field Theory in Statistical Mechanics* translated by R. A. Silverman, (Prentice-Hall Inc., Englewood Cliffs, New jersey, Chap.7, 1963).

[21] C. R. Hu, R. S. Thompson, Dynamic Structure of vortices in Superconductors II $H << H_{c2}$, *Phys. Review B* **6**, 1, p.110 (1972).

[22] A.J.Dolgert, T.Blum, A.T.Dorsey, M.Fowler, Nucleation and growth of the superconducting phase in the presence of a current,*Phys. Review B* **57**, 9, p.5432 (1998).

[23] Q.Du, M.D.Gunzburger, J.S.Peterson, Analysis and approximation of the Ginzburg-Landau model for superconductivity, *SIAM Review*, **34** No.1, pp.54 (1992).

[24] T.P.Orlando, K.A.Delin, *Foundations of Applied Superconductivity*, (Addison-Wesley, Chap. 6-10, 1991).

[25] T.P.Orlando, K.A.Delin, *Foundations of Applied Superconductivity*, (Addison-Wesley, Chap. 7.2, 1991).

[26] R. Kato, Y. Enomoto, S. Maekawa, Effects of the surface boundary on the magnetization process in type-II superconductors, *Phys. Rev. B* **47** 13, p.8016 (1991).

[27] Q.Du, M.D.Gunzburger, J.S.Peterson, Computational simulation of type-II superconductivity including pinning phenomena, *Phys. review B* **51** No.22, p.16194 (1995).

[28] M.Mu, Y.Huang, An alternating Crank-Nicolson method for decoupling the Ginzburg-Landau equations, *SIAM J. Numer Anal.*, **35**, 5, p.1740 (1998).

[29] F.Liu, M.Mondello, N.Goldenfeld, Kinetics of the Superconducting Film, *Phys. Rev. Lett.* **66**, 23, p.3071, (1991).

[30] Y. Enomoto, R. Kato, Computer simulations of a type-II superconductor in a magnetic field, *J. Phys. Condens. Matter* **3**, p.375 (1991).

[31] M. Machida, H. Kaburaki, Direct Simulation of Time-Dependent Ginzburg-Landau Equation for Type-II Superconducting Thin Film: Vortex Dynamics and V-I Characteristics, *Phys. Rev. Lett.* **71**, 19, p.3206, (1993).

[32] L.Lapidus, J.H.Seinfeld, *Numerical Solution of Ordinary Differential Equations*, (Academic press, New York, 1971).

[33] K.Sepehrnoori, *Runge-Kutta formulas with extended regions of stability*, (TICAM report, 78-10, May 1978).

[34] W. B. Richardson, G. F. Carey, and B. J. Mulvaney, Modeling Phosphorus Diffusion in Three Dimensions, *IEEE Trans. on CAD.* **8**, p.487 (1992).

[35] G. F. Carey. *Computational Grids: Generation, Adaptation, and Solution Strategies.* Taylor and Francis, 1997.

[36] A. L. Pardhanani, G. F. Carey, A. Ardelea and W. B. Richardson, *Modeling and Simulation of Ginzburg Landau Models for Superconductivity,* TICAM Report (in preparation), University of Texas, Austin, 2001.

[37] C.Bolech, G.Buscaglia, A.Lopez, Numerical simulation of vortex arrays in thin superconducting films, *Phys. Rev. B* **52**, 22, p.15719 (1995).

[38] G.F.Carey, W.B.Richardson, C.S.Reed, B.J.Mulvaney, Circuit, *Device and Process Simulation*, (John Wiley & Sons , 1996).

[39] M. Machida, H. Kaburaki, Direct Numerical Experiment on Two-Dimensional Pinning Dynamics of a Three-Dimensionnal Vortex Line in Layered Superconductors, *Phys. Rev. Lett.* **75**, 17, p.3178 (1995).

[40] W. D. Gropp, H. G. Kaper, G. K. Leaf, D. M. Levine, M. Palumbo, and V. M. Vinokur, Numerical Simulation of Vortex Dynamics in Type-II Superconductors, *Journal of Computational Physics,* **123**, pp. 254-266 (1996).

[41] F. Bethuel, H. Brezis, F. Hélein, *Ginzburg-Landau Vortices*, (Birkhäuser, 1994).

[42] M. Machida, H. Kaburaki, Structure of Flux Lines in Three-Dimensional Layered Type-II Superconductor: Numerical Experiments, *Phys. Rev. Lett.* **74**, 8, p. 1434 (1995).

[43] J. W. Neuberger, R. J. Renka, Sobolev Gradients and the Ginzburg-Landau Functional, *SIAM J. Sci. Comput.* **20**, pp. 582 (1998).